lubricants

MDPI

Article

Exploring the Tribological Potential of Y_2BaCuO_5 Precursor Powders as a Novel Lubricant Additive

Shuo Cheng, Longgui He and Jimin Xu *

Institute of Tribology, School of Mechanical Engineering, Hefei University of Technology, Hefei 230009, China; chengshuo@mail.hfut.edu.cn (S.C.); helonggui@mail.hfut.edu.cn (L.H.)
* Correspondence: xujimin2017@hfut.edu.cn

Abstract

Friction leads to substantial energy losses and wear in mechanical systems. This study explores the tribological potential of the high-temperature superconductor precursor Y_2BaCuO_5 (Y211), synthesized via chemical co-precipitation, as a novel additive to PAO6 base oil. A 0.3 wt.% Y211/PAO6 lubricant (CD) was formulated using ultrasonic dispersion. Tribological performance was evaluated using a custom end-face tribometer (steel-on-iron) under varying loads (100–500 N) and speeds (300–500 rpm), comparing CD to neat PAO6. The results indicate that the Y211 additive consistently reduced the coefficient of friction (COF) relative to neat PAO6, maintaining a stable value around ~0.1. However, its effectiveness was strongly load-dependent: a significant friction reduction was observed at 100 N, while the benefit diminished at higher loads (>200 N), with the COF peaking around 200 N. Rotational speed exerted minimal influence. Compared with neat PAO6, the inclusion of 0.3 wt.% Y211 resulted in a reduction in the coefficient of friction by approximately 50% under low-load conditions (100 N), with COF values decreasing from 0.1 to 0.045. Wear depth measurements also revealed a reduction of over 30%, supporting the additive's anti-wear efficacy. Y211 demonstrates potential as a friction-reducing additive, particularly under low loads, but its high-load performance limitations warrant further optimization and mechanistic studies. This highlights a novel tribological application for Y211. The objective of this study is to evaluate the tribological effectiveness of Y_2BaCuO_5 (Y211) as a lubricant additive, investigate its load-dependent friction behavior, and explore its feasibility as a multifunctional additive leveraging its superconductive precursor structure.

Keywords: Y_2BaCuO_5; lubricant additive; tribology

check for updates

Received: 23 April 2025
Revised: 2 July 2025
Accepted: 17 July 2025
Published: 19 July 2025

Citation: Cheng, S.; He, L.; Xu, J. Exploring the Tribological Potential of Y_2BaCuO_5 Precursor Powders as a Novel Lubricant Additive. *Lubricants* **2025**, *13*, 315. https://doi.org/10.3390/lubricants13070315

Copyright: © 2025 by the authors. Licensee MDPI, Basel, Switzerland. This article is an open access article distributed under the terms and conditions of the Creative Commons Attribution (CC BY) license (https://creativecommons.org/licenses/by/4.0/).

1. Introduction

With the widespread application of mechanical equipment under extreme conditions and complex operating environments, the critical moving components are increasingly subjected to severe friction and wear due to the coupling effects of multiple physical fields. Such tribological interactions not only lead to the undesirable conversion of mechanical energy into heat, resulting in persistent energy overconsumption, but also significantly reduce equipment lifespan and operational efficiency [1,2]. More critically, unavoidable friction and wear can serve as precursors to safety incidents, posing substantial industrial risks.

As industrial equipment evolves to operate under higher loads, elevated temperatures, and faster speeds, conventional lubrication systems face mounting challenges in both efficiency and durability. Thus, the development of high-performance lubricant additives

has become a major focus in tribology research. Incorporating advanced technologies has been shown to reduce energy losses due to friction by 18–40% [3–5]. Optimizing lubricant systems and selecting appropriate materials can not only extend equipment life and minimize downtime but also reduce environmental pollution.

To mitigate the friction and wear during relative motion between mechanical surfaces [6,7], liquid lubricants have been widely adopted across industrial sectors [8]. In particular, lubricant additives play a pivotal role in enhancing lubrication performance and extending service life. However, under harsh conditions such as high temperature, high pressure, and high speed, traditional lubricants often fail to maintain their performance. Solid additives, in particular, face three major challenges: (1) conventional base oils cannot maintain a stable lubricating film under extreme conditions; (2) solid additives tend to aggregate, leading to poor dispersion and inconsistent inconsistency; and (3) the mechanisms by which additives function under high-pressure contacts remain inadequately understood. Therefore, there is a pressing need for multifunctional additives with thermal stability, effective lubrication, and good dispersibility. To enhance lubrication performance, researchers have recently explored the incorporation of novel functional materials—such as metal particles, metal oxides, graphite, and various nanomaterials—into lubricating oils. These additives exhibit excellent thermal stability, surface activity, and self-healing properties, allowing them to form protective films on frictional surfaces, fill in surface grooves, reduce friction coefficients, and slow down wear progression, ultimately prolonging the service life of mechanical systems [9]. Among these, MXene has been shown to reduce the friction coefficient by more than 35% under a 40 N load, while $Ti_3C_2T_x$-modified particles dispersed in PAO-based oils exhibit excellent thermal stability and boundary lubrication characteristics. The rapid development of nanolubricant additives is injecting new vitality into high-performance lubrication technologies. Strengthening the study of their friction-reducing and anti-wear capabilities is of great scientific value, offering substantial benefits for industrial safety, cost reduction, and economic and social efficiency.

Despite extensive research into metallic and oxide-based additives, the current studies often fall short by focusing mainly on thermally conductive metals or two-dimensional materials, with limited consideration for multifunctional performance. Most investigations are conducted under low-load conditions and thus fail to represent medium- to high-load scenarios.

High-temperature superconductors (HTSs), due to their unique flux pinning-induced levitation and self-stabilization capabilities—achieved without external energy input—can effectively eliminate contact friction in motion. This non-contact mechanism, based on vortex pinning, offers great promise for applications requiring ultra-low friction and long operational lifespans, such as high-speed rotating machinery, magnetic levitation systems, and superconducting motors [10–13]. Over the past three decades, $Y_1Ba_2Cu_3O_{7-x}$ (Y123) has emerged as a prototypical HTS material with well-developed fabrication techniques. The two dominant approaches—powder melting process (PMP) [14] and melt-textured growth (MTG) [15]—have significantly improved the microstructural homogeneity and mechanical performance of Y123-based superconductors. The incorporation of Y_2BaCuO_5 (Y211) as a secondary phase within the Y123 matrix enables a more uniform particle distribution, thereby enhancing the flux pinning effects [16–18].

In light of recent advances in material development for lubrication under extreme conditions, several studies have incorporated HTS materials such as $YBa_2Cu_3O_{7-\delta}$ (YBCO) into self-lubricating composites. Remarkably, a sharp drop in the friction coefficient has been observed near the superconducting transition temperature, spurring discussions on the interplay between Cooper pair decoupling, phonon excitations, and the origin of friction. Dong et al. used quartz crystal microbalance (QCM) techniques and revealed

that in the superconducting state, friction arises primarily from lattice perturbations rather than electron migration. By employing a sol–gel synthesis route, they fabricated finely dispersed $AgNO_3$/YBCO composites that demonstrated stable lubrication behavior up to 500 °C. This characteristic suggests that beyond their electromagnetic applications, YBCO materials hold potential for solid lubrication across wide temperature ranges. However, due to their inherent brittleness, ceramic-based materials like YBCO are often reinforced with metallic silver to improve structural integrity and tribological performance. Ding et al. prepared Ag/YBCO composites via powder metallurgy and observed that a 10% Ag content reduced the friction coefficient to approximately 0.15, with stable behavior under both vacuum and liquid nitrogen environments. Fang et al. [19] further demonstrated through linear reciprocating tests that the friction coefficient between YBCO surfaces is significantly influenced by temperature and humidity, dropping below 0.35 around 400 °C.

To date, however, the tribological potential of Y-series precursor phases such as Y_2BaCuO_5 (Y211) remains largely unexplored. As a key precursor to high-temperature superconductors, Y211 offers excellent thermal stability, surface activity, and structural robustness, yet its application in lubrication has not been systematically studied. Given its favorable particle size control and dispersion characteristics, Y211 is theoretically promising for forming stable load-bearing structures at the frictional interface, thus improving lubrication conditions.

This study, for the first time, proposes the incorporation of Y_2BaCuO_5 precursor particles into a PAO6 base oil as a lubricant additive. The frictional performance and surface interactions under various loads and rotational speeds are systematically investigated. This work represents a pioneering cross-disciplinary application of superconducting precursor materials in tribological lubrication systems. It explores the anti-friction and anti-wear performance of Y211 under diverse operating conditions and investigates the underlying mechanisms via surface morphology analysis. The findings reveal the load-responsive characteristics and film stability of Y211 under medium to high loads, offering new insights into the design of advanced lubricant materials.

2. Materials and Methods

This study focuses on the preparation of Y_2BaCuO_5 (Y211) powder, lubricant formulation, and tribological performance testing. First, high-purity Y211 powder was synthesized by chemical co-precipitation to ensure its structural stability and controllable particle size. Subsequently, 0.3 wt.% of Y211 powder was evenly dispersed in PAO6 base oil to prepare a composite lubricant sample. In order to evaluate the anti-friction and anti-wear performance of the lubricant under different working conditions, a rotating end-face friction test platform based on an annular contact structure was constructed, and systematic tests were carried out under various load and speed conditions. During the experiment, the contact surfaces of the samples were mirror polished to ensure test consistency; the test content included the measurement of friction coefficient, wear depth, and characterization of lubricant viscosity (at 40 °C and 100 °C). This section will introduce the specific details such as the material preparation process, lubricant formulation procedure, experimental platform, and test parameter settings in turn, providing a basis for subsequent result analysis.

2.1. Fabrication of Y211

In the study of Y211 powder synthesis, various methods have been employed to optimize particle size, morphology, and distribution in order to meet the diverse requirements for superconducting applications. These methods mainly include solid-state reaction, chemical co-precipitation, sol-gel processing, and plasma synthesis. Fernández et al. [20] prepared Y211 powder via a combustion synthesis route by mixing nitrates with urea

to initiate a self-sustained exothermic reaction at elevated temperatures. This method reached reaction temperatures up to 900 °C and yielded fine Y211 particles with uniform size distribution and good crystallinity. Owing to its rapid reaction kinetics and localized energy concentration, combustion synthesis favors the formation of high-purity powders with minimal agglomeration.

Zhou et al. [21] optimized the powder reaction pathway by first synthesizing the intermediate phase $BaCuO_2$ through the precalcination of a $BaCO_3$-CuO mixture. This intermediate was then combined with Y_2O_3 in a 1:1 molar ratio and sintered at 900 °C for 14 h in a flowing oxygen atmosphere. The final product was subjected to ball milling to produce ultrafine Y211 powder. This approach significantly improved reaction homogeneity and kinetics, minimized residual unreacted phases, and facilitated the formation of a structurally uniform and fine-grained superconducting precursor. Rotta et al. [22] proposed an innovative approach using solution blow spinning for the synthesis of Y211 nanowhiskers. In this method, a precursor solution of Y211 was ejected through a high-pressure nozzle, forming rapidly moving liquid filaments that solidify as the solvent evaporates in air. The resulting nanowhiskers exhibited high fineness and structural uniformity. This technique enables precise control over the diameter and length distribution of the whiskers while maintaining powder purity, offering excellent processability and tunability.

In this study, the Y_2BaCuO_5 (Y211) precursor powder was synthesized via a chemical co-precipitation method, aiming to obtain fine, compositionally homogeneous, and well-dispersed particles [23,24]. To ensure stoichiometric accuracy, the Y, Ba, and Cu elements were maintained in a molar ratio of 2:1:1. The as-precipitated product, consisting of salt-based compounds, required multiple stages of thermal treatment in a muffle furnace, each followed by ball milling to refine the particle size. The final powder was obtained only after these steps, exhibiting the desired properties. The starting materials included high-purity ($\geq$99.99%) $BaCO_3$, Cu powder, and Y_2O_3. Oxalic acid ($H_2C_2O_4$) was selected as the precipitating agent due to its high reactivity and ability to form stable chelate complexes with metal ions, thereby facilitating the formation of a homogeneous intermediate phase. The synthesis procedure is illustrated in Figure 1. Initially, at room temperature, $BaCO_3$, Cu, and Y_2O_3 were individually dissolved in excess nitric acid (HNO_3) under continuous stirring, resulting in a homogeneous and transparent nitrate solution. During this process, the reaction between $BaCO_3$ and HNO_3 generated CO_2 gas, necessitating careful control of the acid addition rate to prevent vigorous effervescence, which could otherwise disrupt the dissolution and affect solubility. Subsequently, a prepared oxalic acid solution and a moderate amount of aqueous ammonia ($NH_3 \cdot H_2O$) were slowly added dropwise to the nitrate solution under constant temperature. The addition of ammonia served to adjust the pH of the system, ensuring that the precipitation reaction occurred in a mildly acidic environment. The final pH was carefully maintained at approximately 5, a condition favorable for the complete complexation between oxalate ions and metal cations, promoting uniform and controlled precipitation. The mixture was stirred continuously for 15–30 min during precipitation to enhance homogeneity and suppress localized particle agglomeration. Upon completion of the reaction, the precipitate was separated from the supernatant via vacuum filtration. The resulting filter cake was washed repeatedly with deionized water to remove residual nitrates and other ionic impurities and then dried at 100 °C to eliminate moisture and partial organic residues, yielding a light-colored Y211 precursor powder. This precursor was subsequently calcined in air at 900 °C for 10 h, facilitating crystallization and phase formation of Y_2BaCuO_5. During the high-temperature treatment, the residual organics decomposed completely, and oxalate ions combusted to release CO_2 and H_2O. The final product exhibited fine grain size and high crystallinity, with a characteristic green color consistent with the literature-reported features of the Y211 phase. Figure 2 presents

the XRD spectrum of Y211 powder. The pattern indicates a well-defined single phase for the Y211 powder. For the Y211 powder prepared by calcination at 900 °C, the three most prominent peaks observed around 30° 2θ are all indexed to the Y211 phase. The absence of secondary phase peaks confirms the purity of the synthesized Y211. In this study, Y_2BaCuO_5 (Y211) was synthesized as a high-temperature precursor phase and introduced into PAO6 base oil in powder form. Y_2BaCuO_5 exhibits sufficient mechanical strength and thermal stability to endure high-temperature sintering and external stress, which enables it to function as a micro-scale load-bearing additive in lubricating films [25,26]. The tribological behavior of Y211 is closely related to the properties of individual particles rather than bulk characteristics, as the actual contact under boundary lubrication primarily involves discrete micron- and submicron-sized particles. During powder preparation, Y211 particles were found to maintain good morphological integrity after high-temperature calcination, exhibiting rounded edges and structural stability. These features, along with observations of self-lubricating behavior during powder handling, suggest that Y211 particles possess the potential to act as rolling elements at the interface. Previous nanoindentation studies [27] report a nanohardness of approximately 16.7–20.0 GPa for Y211, confirming their mechanical robustness and resistance to deformation or fracture. These characteristics provide the basis for their application as solid lubricant additives in subsequent tribological experiments.

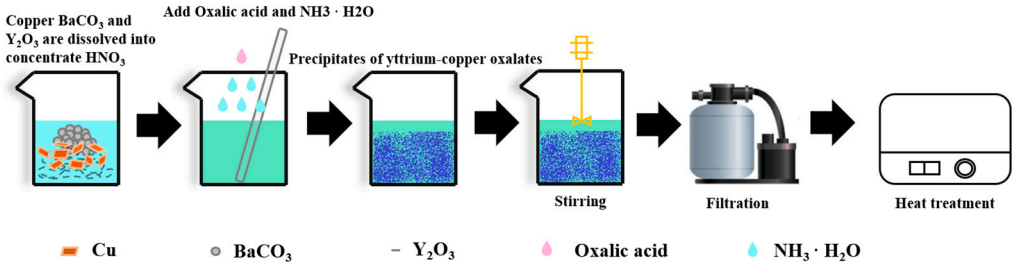

Figure 1. Schematic flowchart illustrating the chemical co-precipitation process for synthesizing Y_2BaCuO_5 (Y211) precursor powder.

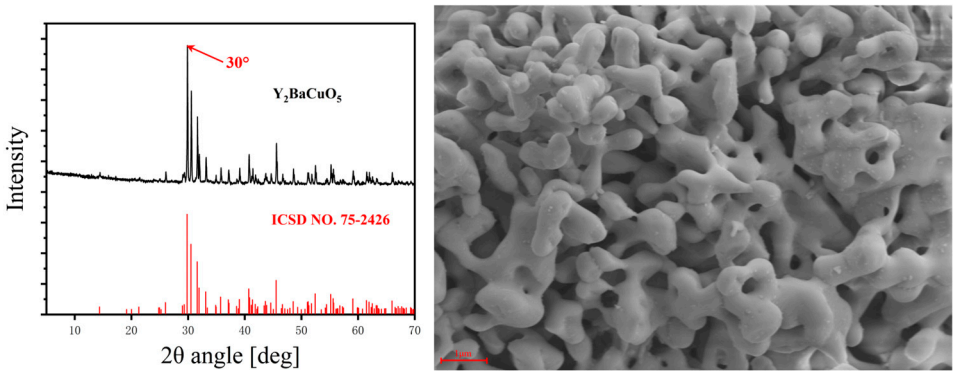

Figure 2. XRD pattern and SEM micrographs of the synthesized Y_2BaCuO_5 (Y211) powder.

2.2. Experimental Methods

The tribological performance of Y211 as a lubricant additive was evaluated experimentally under room temperature conditions. To meet the requirements of experimental precision and customization, a custom-built tribological test platform was employed, with its structural configuration illustrated in Figure 3a. This platform enables controlled and real-time monitoring of the relative motion and applied load between the contact pairs, which makes it suitable for the analysis of lubricant behavior under various operating conditions. The driving unit of the system consists of a stepper motor unit, which is connected to the upper specimen via a coupling. The motor enables high-speed rotation of the upper specimen about a vertical axis, thereby generating face-to-face contact with the

stationary lower specimen. A double-flange torque sensor (model: JNNT-11) regulates the rotational speed of the upper specimen, offering a wide adjustment range for both stepwise and continuous-speed operation according to experimental needs. The loading mechanism comprises an adjustable lifting stage, which applies normal force by vertically displacing the upper assembly to ensure stable contact between the two specimens. The applied load is monitored continuously by a wheel-type force sensor (model: JLBU) mounted on the loading shaft, ensuring accurate and repeatable load application. The sensor output is transmitted in real time to a host computer via a signal acquisition module for further data processing and analysis.

During the measurement, the generated friction torque is measured by the JNNT-11 torque sensor, which is mounted on the transmission shaft. Variations in the torque signal directly reflect the effectiveness of the lubricant in reducing friction under dynamic conditions. All experimental data—including load, rotational speed, and frictional torque—are continuously recorded by a computerized control system and exported for subsequent calculation of the friction coefficients and wear trends. The design of this custom-built tribological test platform is intended to ensure experimental stability, measurement precision, and data traceability. It provides a reliable setup for investigating the tribological behavior and lubrication performance of Y211-based liquid lubricants under face-to-face contact conditions. All test parameters were maintained at a constant throughout the experiments to ensure result repeatability and reliability.

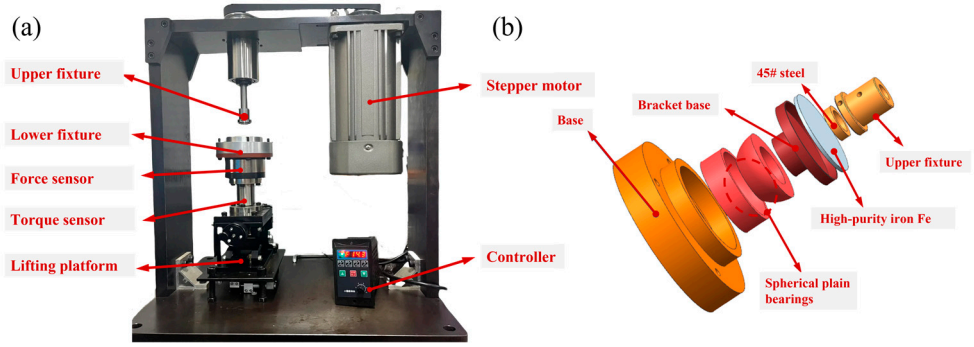

Figure 3. Schematic of the custom-built friction and wear test platform (**a**) and the structural configuration of the tribological interface assembly (**b**).

As shown in Figure 3b, the experimental setup incorporated a self-aligning spherical bearing in the upper assembly to ensure stable contact between the test specimens during the loading process. This structural feature maintained consistent interface engagement throughout the friction and wear tests, thereby enhancing the reliability of load transmission. A ring-shaped specimen made of 45# steel was used as the upper sample, while a high-purity iron disc served was used as the lower specimen, forming a ring-on-disc tribological pair. This configuration was designed to evaluate the tribological performance of Y211-based lubricants at a steel–iron interface. To further enhance contact conformity and uniform load distribution across the frictional interface, the base and support structures were machined from high-strength alloy materials, providing enhanced rigidity and vibration. This design effectively reduced the influence of mechanical vibrations on data accuracy. Additionally, the entire test assembly was constructed in a modular form, allowing for easy disassembly and specimen replacement while facilitating comparative testing under various lubrication conditions.

To ensure the reliability of the data obtained, the custom-built end-face friction and wear tester used in this study was benchmarked against a commercial tribometer. Comparative validation experiments were performed using an HDM-20 end-face friction and wear tester. The mechanical configuration and contact design of the HDM-20 are functionally

equivalent to those of the self-developed system, which allows for consistent contact mechanics between the two setups. In both systems, the upper specimen was a 45# steel ring, and the lower specimen was a DT4C-grade high-purity iron disc. The test configuration and parameters were kept identical throughout all comparative runs. Friction coefficients were recorded under the same loading and rotational speed conditions. The results showed that the average deviation in measured friction coefficients between the two devices was within 10%. This variation is considered acceptable in tribological practice, where factors such as frame stiffness, alignment, and dynamic response often result in small discrepancies. The agreement between the two systems confirms that the custom-built tribometer provides sufficient precision and stability for research-grade tribological analysis.

2.3. Preparation of Lubricating Oil

Before conducting the full set of tribological evaluations, a preliminary test was carried out to explore the influence of Y_2BaCuO_5 (Y211) concentration on the friction performance of the CD lubricant. This experiment aimed to identify a suitable concentration range and determine the optimal additive content for stable and low-friction operation under boundary lubrication conditions. To this end, three CD formulations were prepared with Y211 mass fractions of 0.1 wt.%, 0.3 wt.%, and 0.5 wt.%, respectively. All tests were conducted under consistent conditions—100 N normal load and 400 rpm rotational speed. The friction coefficient (COF) results are shown in Figure 4.

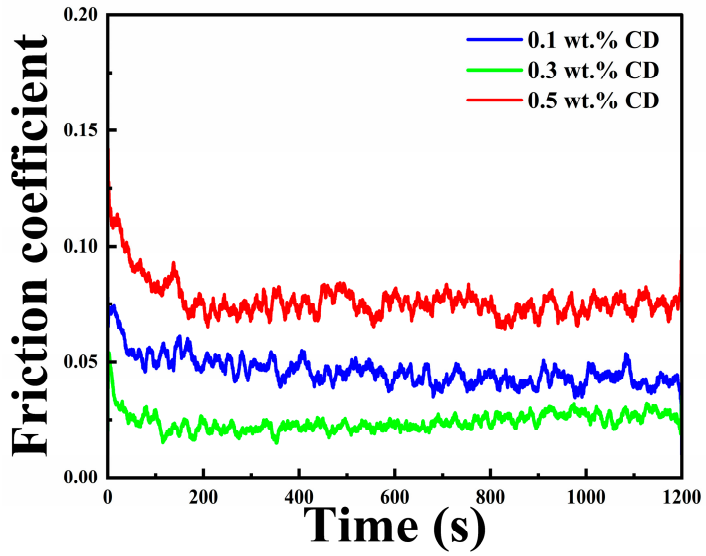

Figure 4. Friction properties of Y211. The load was 100 N, speed was 400 rpm, and friction time was 20 min.

Among the three groups, the 0.3 wt.% CD sample exhibited the lowest and most stable COF. This suggests that at this concentration, Y211 particles are well-dispersed and effectively contribute to the formation of a continuous boundary lubricating film. In comparison, the sample with 0.1 wt.% Y211 exhibited a slightly higher average coefficient of friction (COF) of approximately 0.05. This may be attributed to insufficient particle coverage at the contact interface, resulting in poor film continuity and limited load-bearing effectiveness. On the other hand, the 0.5 wt.% sample may have performed poorly due to excessive particle content leading to agglomeration, which disrupted lubricant flow and introduced localized abrasive interactions. These observations confirm that the friction-reducing effect of Y211 is concentration-sensitive. Both under-dosing and overdosing can negatively impact lubrication efficiency. Based on its relatively stable and favorable friction behavior under preliminary test conditions, the 0.3 wt.% formulation was selected as the

working concentration for all subsequent experiments in this study, including systematic evaluations under varying loads and speeds, as well as post-test surface characterizations.

To evaluate the dispersion stability and reusability of Y211 powder as a lubricant additive, a 0.3 wt.% Y211-in-PAO6 suspension was prepared, hereafter referred to as CD. In this formulation, high-purity Y211 powder serves as the solid additive, while PAO6 acts as the base oil. Due to the strong inherent tendency of Y211 particles to agglomerate, spontaneous clustering readily occurs upon their introduction into the PAO6 matrix, resulting in large aggregate formation. This aggregation behavior significantly impairs the additive's anti-friction and anti-wear performance at the tribological interface. However, owing to its hydrophobic nature, Y211 can be readily dispersed in PAO6 following prolonged ultrasonic treatment. To achieve a uniform and stable suspension, the mixture was subjected to ultrasonic dispersion. The cavitation and shear forces generated by ultrasonication effectively disintegrate agglomerates, promoting a well-dispersed and stable distribution of solid particles within the lubricant. Following appropriate pre-treatment, Y211 demonstrates a sustained dispersion stability in PAO6, highlighting its potential for practical lubricant applications.

To evaluate the dispersion state of Y_2BaCuO_5 (Y211) particles in PAO6 base oil, dynamic light scattering (DLS) measurements were performed using a Zetasizer instrument. As shown in Figure 5, the particle size distribution curves of three independent samples (Y211 PAO6 01–03) exhibit a sharp and consistent peak, with unimodal peaks centered at approximately 468.4 nm, 538.9 nm, and 636.3 nm. The corresponding Z-average diameters ranged from 404.7 to 570.4 nm, with polydispersity index (PdI) values between 0.646 and 0.719. These values indicate a moderately narrow size distribution and good batch-to-batch reproducibility. The relatively uniform size profiles suggest that the Y211 particles were well-dispersed within the PAO6 matrix, without the presence of significant agglomerates. According to Peña-Parás et al. [28], particles smaller than the average surface roughness are more likely to penetrate valleys and reduce friction and wear. In our case, the Y211 particles (400–600 nm) are comparable to or smaller than the measured roughness (Ra $\approx$ 0.7–1.2 μm), supporting their potential as active tribological agents. This indicates high dispersion uniformity and inter-batch reproducibility. Additionally, no significant sedimentation was observed within 12 h of sample preparation under room-temperature conditions, and the suspension was fully redispersed after 10 min of mild ultrasonication, indicating favorable dispersion stability and reusability of the Y211-PAO6 system. A noticeable difference was observed between the particle sizes measured by scanning electron microscopy (SEM) and those obtained by dynamic light scattering (DLS). This discrepancy can be explained by the inherent differences in testing state and measurement principles. SEM is a dry-state, surface-imaging technique. During sample preparation, particles can agglomerate or stack due to van der Waals forces and capillary action as the solvent evaporates. In contrast, DLS is a wet-state, dynamic method based on the diffusion behavior of particles in suspension. It is sensitive to hydrodynamic diameter and relies on good optical transparency of the dispersing medium—in this case, PAO6 base oil. The DLS results revealed a narrow and consistent size distribution for the Y211 particles, with no signs of large-scale agglomeration, indicating good dispersion stability under functional lubrication conditions.

The viscosity of the prepared lubricant oil was tested by rotational rheometry at 40 °C and 100 °C. As shown in Figure 6, the viscosity decreased initially and then stabilized at both temperatures, indicating mild shear-thinning characteristics typical of particle-filled lubricant systems. This transition to a stable flow regime under high shear is likely due to the structural alignment or rearrangement of Y211 particles within the fluid matrix. Shear stability is essential for maintaining consistent lubrication performance at high rotational speeds, as it ensures uniform film formation and reduces flow resistance. The lubricant

began to evaporate at 40 °C and exhibited greater evaporation at 100 °C. Throughout the tests, no thermal degradation phenomena—such as lubricant discoloration, smoke, odor, or signs of melting—were observed. In addition, the friction coefficient curves remained stable over the entire duration of each test, with no indication of thermal drift. Therefore, it is reasonable to conclude that frictional heating had minimal influence on the measured friction and wear behavior in this study.

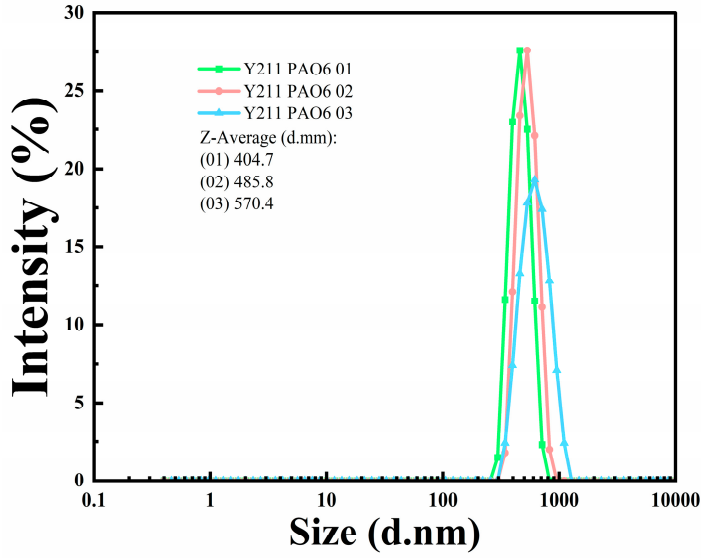

Figure 5. Particle size distribution of Y_2BaCuO_5 dispersed in PAO6 base oil.

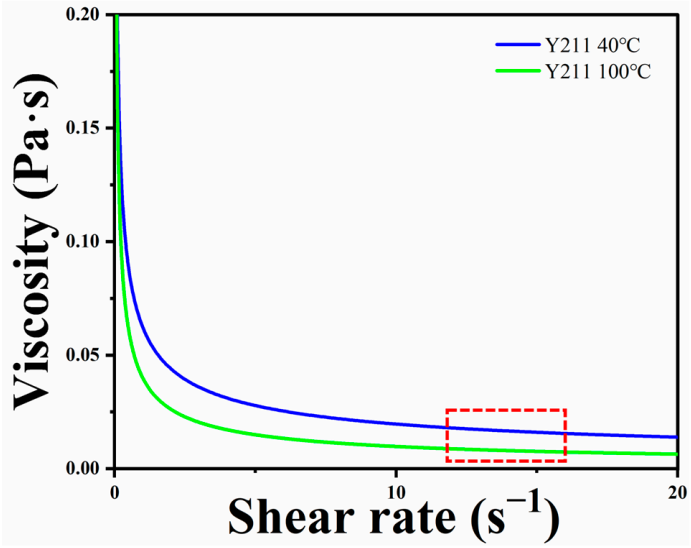

Figure 6. Shear-rate-dependent viscosity profiles of Y211-based lubricants at 40 °C and 100 °C.

Over time, the system gradually developed visible sedimentation, eventually leading to the accumulation of particles at the bottom of the container as a discernible sediment layer. As shown in Figure 7a, after ultrasonic treatment, the dispersion showed a greenish suspension, indicating good initial dispersibility. However, with increasing standing, the upper layer of the dispersion gradually became clear, and obvious sedimentation appeared at the bottom, indicating that the particles slowly sank under the action of gravity. Sedimentation onset was observed at approximately 18 h and completed by 96 h. This sedimentation is considered a reversible physical process, rather than a result of irreversible aggregation or chemical degradation. A brief ultrasonic treatment is sufficient to re-disperse the settled particles, restoring the uniformity and flow characteristics of the

lubricant. As shown in Figure 7b, after 10 min of mild ultrasonication, the suspension returned to its original homogeneous state, demonstrating excellent redispersibility. This reversible dispersion–settling–redispersion behavior exhibits good repeatability and ease of operation, demonstrating the stable dispersibility of Y211 in PAO6 and its suitability for repeated or cyclic lubrication applications.

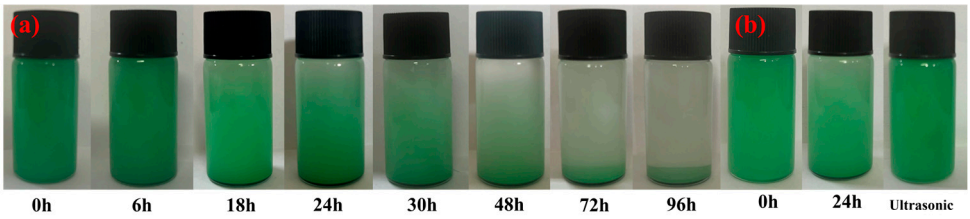

Figure 7. Time-dependent settling behavior of Y211 particles in PAO6 base oil following ultrasonic dispersion: (**a**) Settling behavior observed over time after initial ultrasonic dispersion; (**b**) Settling behavior after prolonged standing followed by a subsequent 10-minute ultrasonic dispersion.

2.4. Rotation Tribological Evaluation Using End-Face Contact Geometry

Before initiating the end-face rotational tribological experiments, rigorous surface preparation of all test specimens was conducted to ensure the precision, consistency, and reliability of the resulting data. The upper specimen was a 45# steel ring with an outer diameter of 20 mm and an inner diameter of 14 mm. The effective contact area with the lower sample is about 1.602×10^{-4} m^2, while the lower specimen was a high-purity iron (Fe > 99.9%) disc, specifically grade DT4C. Both the upper and lower specimens were mechanically polished to a mirror-like finish, with a measured surface roughness (Ra) of 0.06 μm, ensuring a low and uniform surface roughness and eliminated surface defects such as scratches, pits, or embedded debris, which are known to interfere with tribological performance and introduce noise into the data. Following mechanical polishing, all specimens were subjected to ultrasonic cleaning in anhydrous ethanol to remove residual oils, surface particulates, and any contaminants introduced during sample handling or polishing. This step was essential to avoid uncontrolled variables that could distort the measured friction and wear behavior, particularly when assessing lubricant effectiveness. The tribological tests were conducted with a constant applied load and rotational speed maintained throughout each run, using a force sensor (JLBU) and a torque sensor (JNNT-11). The duration of each test was uniformly set to 20 min to ensure data comparability across all test conditions. The normal load was varied from 100 N to 500 N in discrete increments of 100 N, resulting in five distinct loading conditions, corresponding to a contact pressure of 0.62 MPa to 3.12 MPa. The lower specimen remains stationary, while the upper specimen rotates at speeds of 300, 400, and 500 rpm (corresponding to 0.267 m/s, 0.356 m/s, 0.445 m/s, respectively), the selected normal loads and corresponding contact pressures fall within the range reported in previous studies using oxide-based or ceramic nanoparticle additives. For example, Serre et al. [29] used a ring-on-disk configuration under comparable conditions to evaluate the effect of graphite-based materials. An orthogonal test matrix was constructed to explore the interaction effects between load and speed, thereby enabling comprehensive coverage of key frictional regimes. Each experimental condition was repeated three times to ensure reproducibility and to minimize the influence of outliers and random variability. Due to the inherent variability in tribological systems, slight differences were observed among the replicates. To reduce the influence of outliers and maintain consistency in trend interpretation, a trimmed mean selection strategy was employed. Specifically, the three friction coefficient curves were compared based on their values, and the curve with the median value (i.e., between the highest and lowest) was selected. These repeated trials also allowed for statistical averaging and improved the robustness of the

conclusions drawn from the data. The experimental setup was developed to serve as a stable and functional platform for evaluating the tribological behavior of the lubricant system under end-face rotational sliding. Its configuration supports consistent loading and motion control, enabling the systematic investigation of friction and wear characteristics under well-defined operating conditions.

All tests were performed under boundary lubrication conditions. Prior to each test, 5 mL of the prepared lubricant was applied uniformly to the entire surface of the stationary lower specimen using a calibrated pipette. Lubricant was applied only once at the beginning of the test, with no additional oil supplied during operation. For repeatability, both the upper and lower specimens were thoroughly cleaned and re-lubricated before each repeated test, ensuring consistent lubrication conditions across all trials. The tribological tests were conducted under ambient laboratory conditions, with the temperature maintained at room temperature, typically ranging from 22 °C to 26 °C throughout the experiments. All tests were carried out in a controlled environment without intentional external heating or cooling, ensuring consistent thermal conditions across different runs. This step was essential for establishing a consistent initial lubrication condition across all experimental runs. Upon commencement of the friction test, the apparatus automatically recorded the real-time evolution of the coefficient of friction (COF) along with the applied load, yielding a continuous dataset for subsequent analysis of frictional stability and lubrication performance. Each test was conducted for a fixed duration of 20 min, which was selected to simulate typical short-term sliding conditions and to enable consistent evaluation of lubricant performance across all test conditions. After completion of the experiment, both the upper and lower specimens were thoroughly cleaned using anhydrous ethanol to remove any residual lubricant, debris, or wear particles. This post-test cleaning procedure ensured a clean, residue-free surface suitable for subsequent microscopic surface characterization or quantitative wear volume analysis.

The coefficient of friction (COF) was calculated based on the torque and normal force data acquired during testing. The torque sensor and the force sensor were integrated into the test system to continuously monitor the frictional torque (T) and applied normal load (F_n), respectively. The COF was derived using the following classical relation:

$$\mu = \frac{T}{F_n \cdot r}$$

The μ is the coefficient of friction (dimensionless); T is the measured frictional torque (N·m); F_n is the applied normal load (N); and r is the effective contact radius (m). The ring specimen had an outer radius of 10 mm and an inner radius of 7 mm, resulting in an effective contact radius r calculated as the mean of the two: $r = \frac{R_0+R_i}{2} = 8.5$ mm.

All tribological tests were performed under ambient conditions. Given the moderate loads, low sliding speeds, and short test durations, the frictional heating was expected to be minimal. No signs of thermal degradation (e.g., lubricant discoloration or abnormal wear) were observed, and friction curves remained stable. Therefore, temperature effects were considered negligible in this study.

3. Results

After completing the experiment, the coefficient of friction profiles under different experimental conditions were obtained, highlighting the substantial tribological improvements resulting from the incorporation of 0.3 wt.% Y211 additive formulation into the PAO6 base oil. The data reveal a consistent reduction in COF upon incorporation of the additive, demonstrating its effectiveness in improving lubrication performance, reducing frictional losses, and potentially extending the service life of the lubricant. Notably,

across the tested range of normal loads and rotational speeds, the COF of the unmodified PAO6 remains stable, with values fluctuating narrowly around 0.1. This behavior reflects the inherent stability of PAO6 and its capability for maintaining consistent lubrication under varying mechanical conditions.

In contrast, the Y211-modified system (CD) demonstrates a more complex and non-linear frictional behavior. As shown in Figure 8, when rotational speed is held constant, the COF of CD initially rises with the increasing load, reaches a peak at 200 N, and then declines slightly with a further load increase, before rising again at higher loads. This trend reflects the complex interaction between the applied load and boundary film behavior. At lower loads, CD outperforms the base oil significantly, exhibiting enhanced friction-reducing capability—likely attributable to the efficient formation of a stable boundary film aided by the uniform dispersion of Y211 nanoparticles. These particles may contribute to improved load distribution and micro-rolling or sliding effects at the interface, thus lowering interfacial shear resistance.

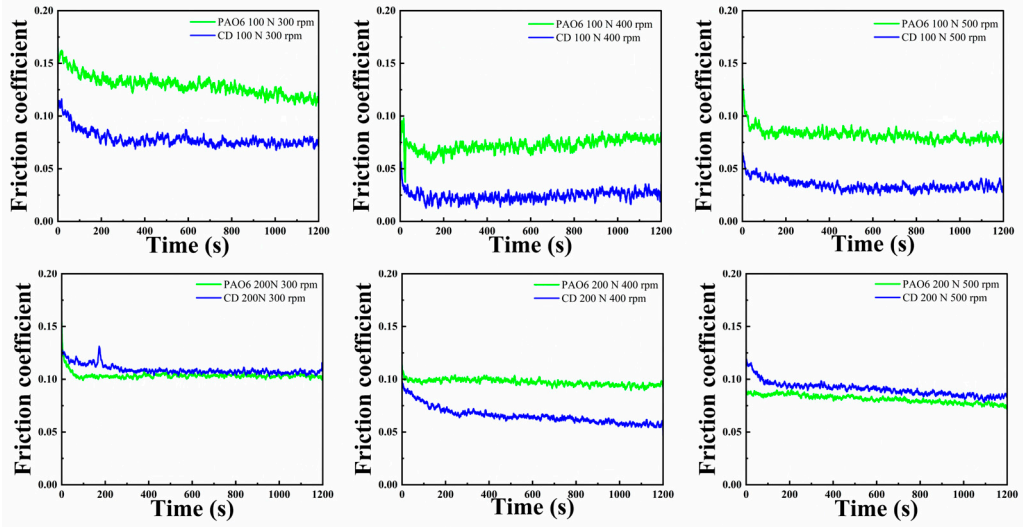

Figure 8. Comparison of friction coefficients under 100 N and 200 N loads at different rotational speeds.

However, the performance of CD declines at intermediate loads, where the COF reaches its maximum. This anomalous rise in friction may be attributed to the localized breakdown or destabilization of the lubricating film under mechanical stress, coupled with limited replenishment of additive particles within the contact interface. When the load exceeds 200 N, as shown in Figure 9, the COF decreases again, indicating a partial recovery of film stability or increased lubricant redistribution, yet the advantage over pure PAO6 becomes negligible. At higher loads, the extrusion of the lubricant from the contact zone becomes more pronounced, potentially hindering the additive's ability to maintain sufficient presence at the frictional interface. Consequently, the tribological behavior is increasingly governed by the base oil's intrinsic film-forming capability rather than by additive-mediated effects.

Furthermore, variations in rotational speed—while keeping the load constant—have only a limited effect on the COF. A slight decrease is observed at elevated speeds, possibly due to increased lubricant mobility, accelerated film reformation, and enhanced thermal dissipation. Nevertheless, the minor extent of this effect suggests that rotational speed is not a primary factor governing frictional behavior in this system. Instead, the data indicate that applied load and the physicochemical characteristics of the additive play a dominate role in governing frictional behavior.

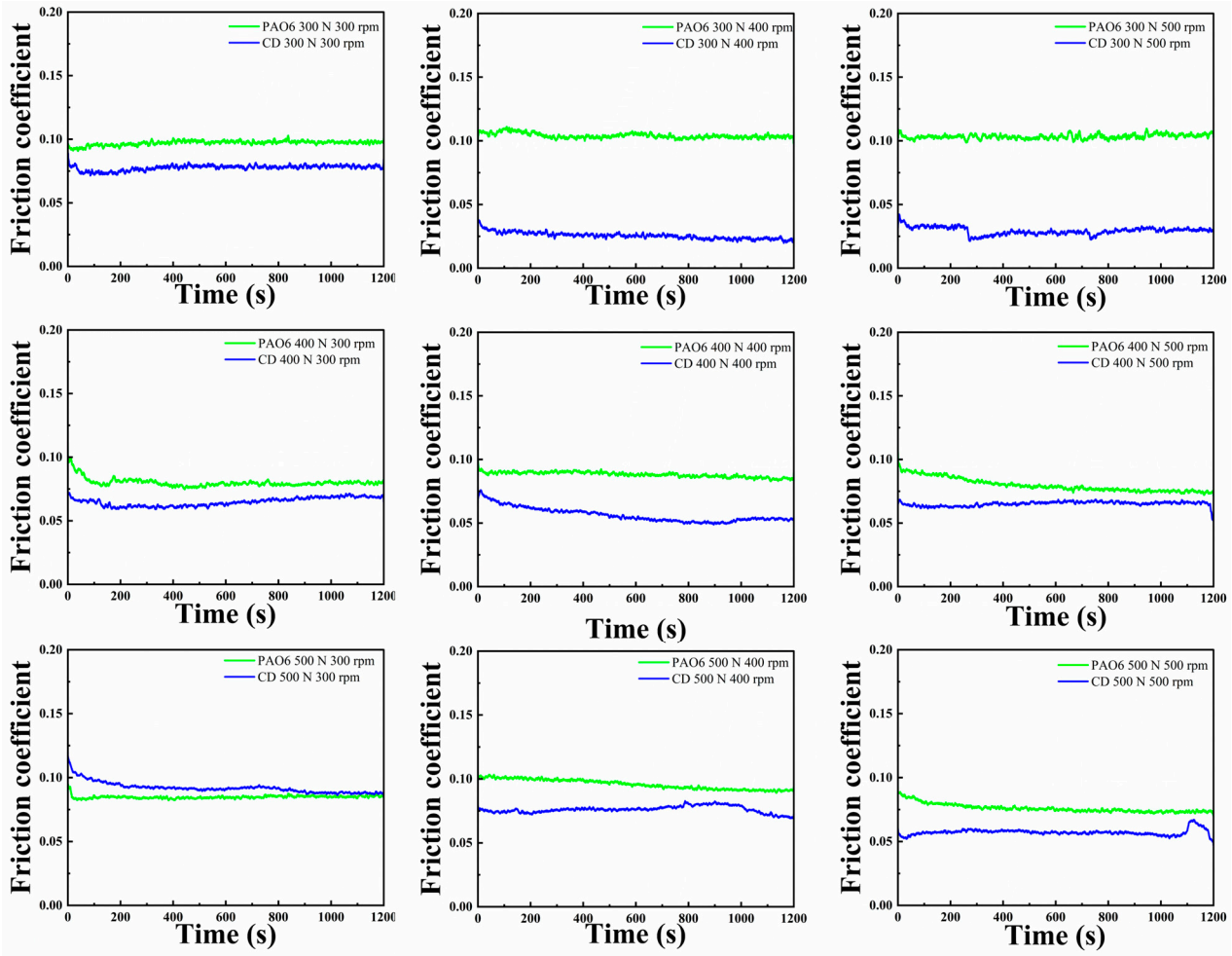

Figure 9. Comparison of friction coefficients under 300 N to 500 N loads at different rotational speeds.

To ensure statistical reliability and assess the repeatability of the tribological results, each load–speed combination was tested in triplicate. The average coefficient of the friction values and corresponding standard deviations are presented in Figure 10 for the Y_2BaCuO_5 lubricant (CD) and the PAO6 base oil, respectively.

As shown in Figure 10, the CD lubricant demonstrated a substantial reduction in COF, particularly under low-load conditions (100 N), where the average COF dropped below 0.05. However, under intermediate loads (200–300 N), moderately increased standard deviations were observed, indicating variability in boundary film formation and stability. This behavior is likely attributable to localized shear-induced film disintegration or incomplete replenishment of the additive particles at the frictional interface, which may temporarily impair the load-carrying capacity and result in frictional fluctuations. At higher loads (400–500 N), the variance decreased again, suggesting that the system reached a more uniform tribological regime, possibly governed by bulk lubricant flow and stabilized surface interactions. In contrast, the PAO6 base oil maintained a higher and more uniform COF (typically 0.08–0.13), with relatively small error bars across all tested conditions. This reflects the absence of active film-forming constituents in the base oil and its limited ability to adapt to mechanical stress or shear rate variations. The inclusion of standard deviation bars enables the direct assessment of data reproducibility and confirms that the observed trends are statistically significant. Moreover, the load-dependent variability in the CD system underscores the interplay among additive dispersion, shear stability, and film integrity—key factors governing nanoscale lubrication mechanisms. This demonstrates

that Y_2BaCuO_5 exhibits measurable, load-sensitive friction-reducing behavior while also revealing its potential limitations under dynamic or high-load conditions.

Overall, the experimental results reveal a nuanced picture: the CD formulation exhibits significant friction-reducing benefits under low-load conditions, where boundary lubrication induced by the additive is most pronounced. However, as the load increases, the performance gains diminish, and the system ultimately performs similarly to the unmodified PAO6. These findings underscore the need to understanding additive–substrate interfacial interactions, lubricant film integrity, and load-driven dynamic effects in the design of high-performance lubricants tailored for variable operating demands.

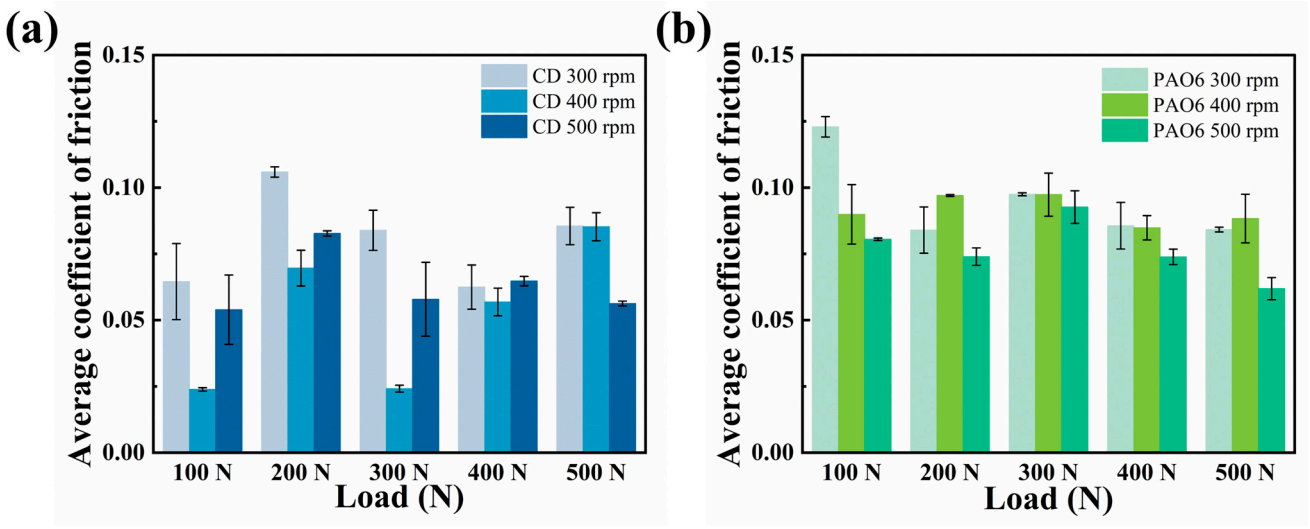

Figure 10. Average coefficient of friction and standard deviation for CD and PAO6 lubricants under different loads and rotational speed conditions: (**a**) Average coefficient of friction of CD-containing lubricant under varying loads and rotational speeds; (**b**) Average coefficient of friction of PAO6 base oil under the same operating conditions.

To further investigate the anti-wear mechanisms afforded by the Y211 lubricant additive under different loading conditions, three-dimensional surface morphology analyses of the tribological contact areas were performed using laser confocal microscopy. Combined with the friction coefficient data, these observations offer insight into the formation stability and continuity of the lubricating film at the microscopic level, especially under different loading conditions. For comparative purposes, two representative conditions—associated with notable reductions in COF—were selected for further microstructural analysis, as shown in Figure 11.

Under the 100 N load condition at 400 rpm, the worn surface exhibits a relatively smooth topography, devoid of large-scale adhesive patches or severe material delamination. Only slight, directionally aligned wear marks are observed, consistent with minor abrasive wear and aligned with the rotational motion of the end-face configuration. The surface profile exhibits a maximum height variation of approximately 177 μm, indicating moderate material removal. Notably, the coefficient of friction remains low and stable, ranging from 0.035 to 0.045 under lubrication with the Y211-enhanced oil (CD), demonstrating the additive's ability to facilitate the formation of a stable and effective boundary film. This performance significantly surpasses that of the base oil (PAO6), thereby confirming the additive's efficacy in reducing interfacial shear and suppressing wear under mild loading conditions. At an elevated load of 300 N, while the rotational speed remains constant, the contact interface is subjected to substantially higher normal stress, leading to increased shear force and thermal accumulation. Under this condition, localized groove-like wear features emerge, suggesting localized surface damage. However, these features

are non-uniform and primarily confined to discrete regions, likely attributable to uneven load distribution or imperfect fixture alignment during the tribological test. These outlier regions were excluded from the quantitative evaluation. The remainder of the surface still exhibits a degree of morphological continuity, with no signs of catastrophic tearing or large-scale material detachment. The COF remains consistently low range (0.035–0.045), implying that the Y211 additive retains its film-forming capability and delivers measurable tribological benefit even under intensified mechanical loading. The observed film resilience and resistance to shear-induced failure suggest that although partial film breakdown may occur at localized points, the overall lubricating system maintains functional integrity and prevents the full-scale failure of the lubrication regime.

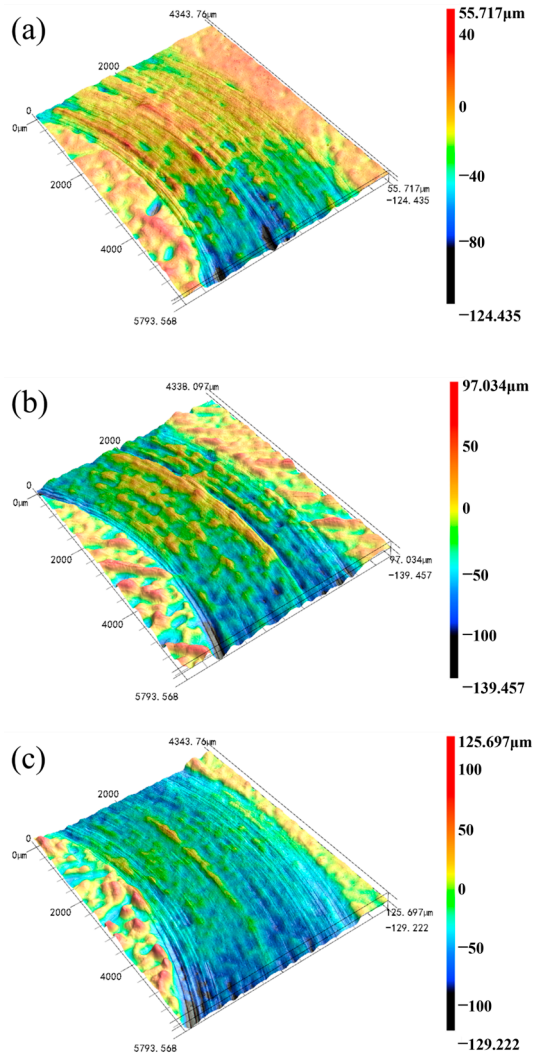

Figure 11. Three-dimensional surface morphologies of wear tracks under different experimental conditions: (**a**) CD 100 N 400 rpm; (**b**) CD 300 N 400 rpm; (**c**) PAO6 100 N 400 rpm.

As shown in Figure 11c, under the operating condition of 100 N load at 400 rpm, the worn surface under PAO6 lubrication reveals a distinct morphology characterized by elongated, groove-like features aligned with the direction of rotational motion. These grooves are relatively uniform and continuous, indicating a stable shear interaction at the sliding interface throughout the test duration. The dominant wear mechanism is primarily attributed to ploughing and micro-abrasive wear, where micro-cutting and third-body particle detachment have resulted in material loss. Importantly, the maximum measured

wear depth under PAO6 lubrication exceeds that observed with the CD formulation, indicating inferior anti-wear capability in comparison.

In terms of frictional behavior, the coefficient of friction (COF) initially records a value of approximately 0.135, corresponding to the initial stage of boundary film formation. As the test progresses, particularly beyond the 600 s mark, a progressive decline in COF is observed, eventually stabilizing around 0.10. This trend reflects the development of a partially continuous boundary film capable of mitigating interfacial shear and reducing frictional losses. Although PAO6 exhibits some boundary film-forming capability under this mild loading condition, its overall tribological protection is inferior to that of the Y211-enhanced formulation, particularly regarding wear suppression and sustained friction reduction over time.

As shown in Figure 12, the wear rate was determined by averaging the cross-sectional areas from 100line scans of the wear scar [25,30,31]. The cross-sectional areas were automatically calculated using the VK-X Series program. The specific wear rate (WR) in this study was calculated using a standardized geometric method, based on the measured wear volume, applied normal load, and total sliding distance. The formula used is the following:

$$WR = \frac{V}{F \cdot S} \tag{1}$$

V is the wear volume (mm^3); F is the applied normal load (N); S is the total sliding distance (m), calculated as: $S = 2\pi R \cdot N \cdot t$, where R is the mean radius of the wear track, N is the rotational speed (revolutions per minute), and t is the total test duration in minutes. Wear volume V was obtained by integrating the measured cross-sectional area of the wear scar over the full circumference. The corrected wear rate values now fall within the typical range for oxide-based nanoparticle lubricant systems (10^{-5} to 10^{-6} $mm^3/N \cdot m$), which are far below the severe wear threshold of 10^{-3} $mm^3/N \cdot m$.

When the CD formulation was applied as the lubricant, the wear rates under load forces of 100 N and 300 N at a rotational speed of 400 rpm were 6.46×10^{-5} $mm^3/N \cdot m$ and 3.29×10^{-5} $mm^3/N \cdot m$, respectively. When PAO6 was used as the lubricant under a 100 N load at 400 rpm, the wear rate was 10.52×10^{-5} $mm^3/N \cdot m$. The wear rate observed with CD lubrication is significantly lower than that of PAO6, indicating superior anti-wear performance.

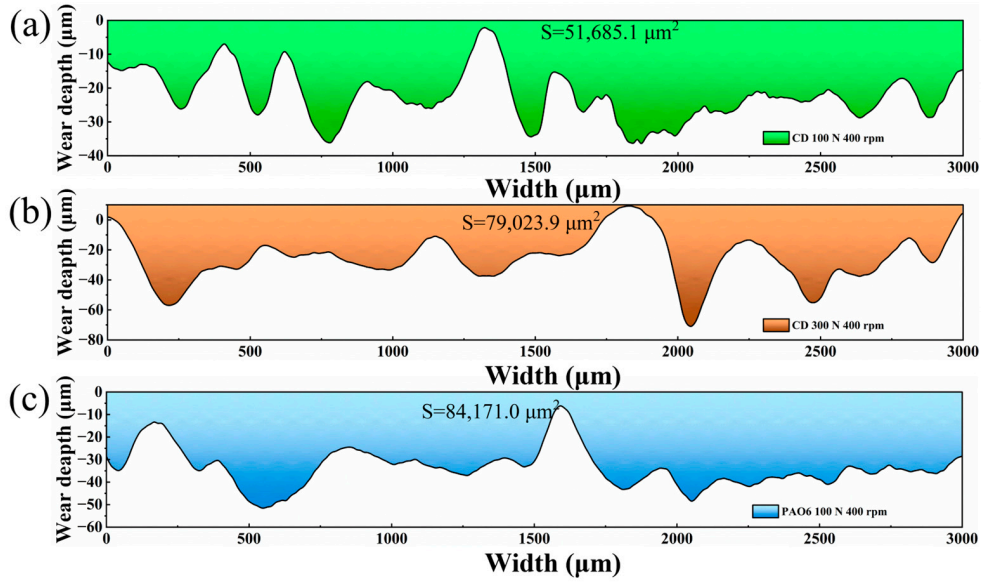

Figure 12. Cross-sectional areas of wear marks tested at (**a**) CD 100 N 400 rpm, (**b**) CD 300 N 400 rpm, (**c**) PAO6 100 N 400 rpm.

Figure 13 presents SEM images of the worn surfaces under different lubrication and loading conditions, all captured at a magnification of 1000×. Figure 13a represents the condition of 100 N at 400 rpm using Y_2BaCuO_5 as a lubricant additive; Figure 13b represents 300 N at 400 rpm with the same additive; and Figure 13c illustrates the worn surface under 100 N at 400 rpm using neat PAO6 base oil. As shown in Figure 13a, the wear surface under low-load conditions with the Y211-enhanced lubricant appears relatively smooth, exhibiting only shallow grooves and minimal abrasive wear features. This observation aligns with the low coefficient of friction and wear rate recorded under this condition, suggesting the formation of a stable boundary lubrication film. The dispersed Y211 particles likely contributed to this effect by filling surface asperities and resisting interfacial shear stress. In contrast, Figure 13b reveals significantly more pronounced grooves and ploughing scars at the higher load of 300 N, even with the same Y211 additive. These morphological changes indicate intensified abrasive action and localized breakdown of the lubricating film, implying that the anti-wear performance of the Y211 system exhibits load-dependent behavior. While the COF remained relatively low, the increased mechanical stress may have compromised the structural stability of the lubrication film, leading to performance deterioration. Figure 13c, representing the condition using only PAO6 base oil at 100 N, displays a rougher surface with wider wear tracks and more evident signs of adhesive and abrasive wear. This condition recorded a higher coefficient of friction (~0.1) and greater wear rate, confirming the inferior anti-wear capability of the base oil in the absence of functional additives.

To further elucidate the role of Y211, EDS analysis was performed on the worn surfaces. Y_2BaCuO_5 (Y211) particles exhibit high hardness and excellent thermal stability. When uniformly dispersed within the oil matrix, these micro- to nano-scale particles can function as solid micro-bearings or spacers at the frictional interface, thereby reducing the actual contact area and redistributing the applied load across micro-asperities. This mechanism is characteristic of ceramic-based lubricant additives and contributes significantly to friction and wear reduction.

As shown in Figure 14, EDS analysis of the surface lubricated by the Y211-containing oil under 100 N revealed the presence of yttrium (0.26 wt.%) and oxygen (2.05 wt.%), even after ultrasonic cleaning in anhydrous ethanol. This indicates that a portion of the Y211 particles or tribo-chemical reaction products remained adhered or embedded on the contact surface, forming a protective tribofilm that helps minimize direct metal-to-metal contact. Although Y211 lacks the lamellar structure of traditional solid lubricants such as MoS_2 or graphite, its stable oxide lattice and low chemical reactivity can help suppress oxidation-induced adhesive wear. Additionally, its reported hydrophobic nature may reduce interfacial free energy and facilitate shear accommodation, further enhancing boundary lubrication performance.

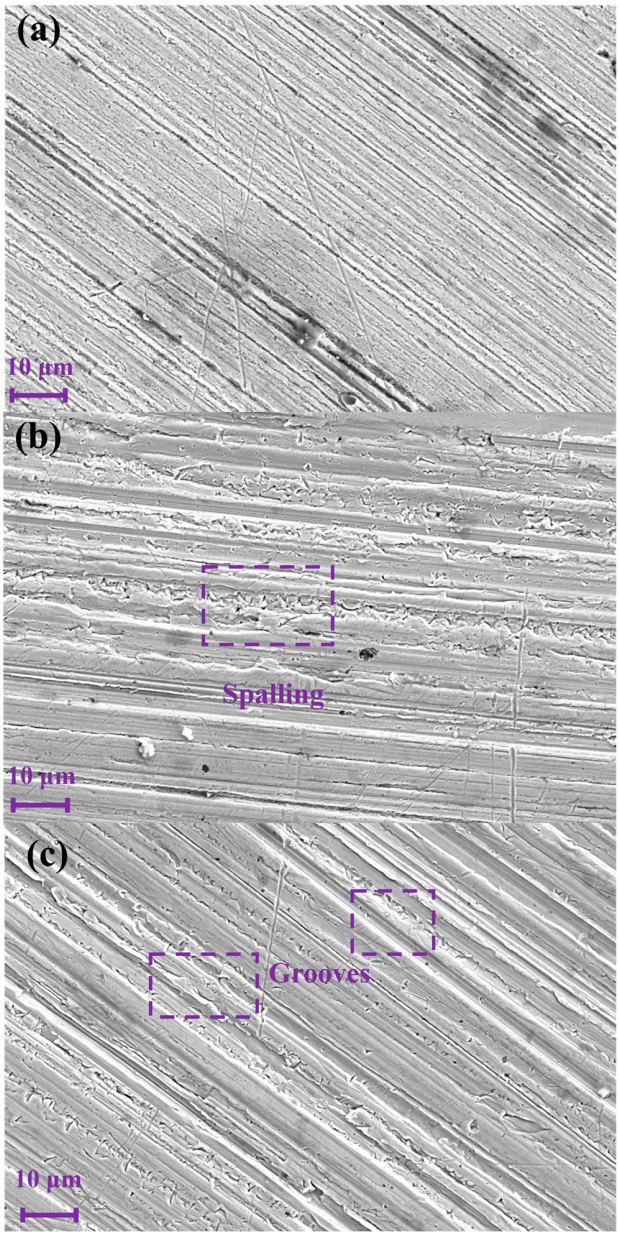

Figure 13. SEM images of worn surfaces under different lubrication and loading conditions, magnified at 1000×: (**a**) CD lubricant (Y211 additive), 100 N, 400 rpm; (**b**) CD lubricant, 300 N, 400 rpm; (**c**) PAO6 base oil, 100 N, 400 rpm.

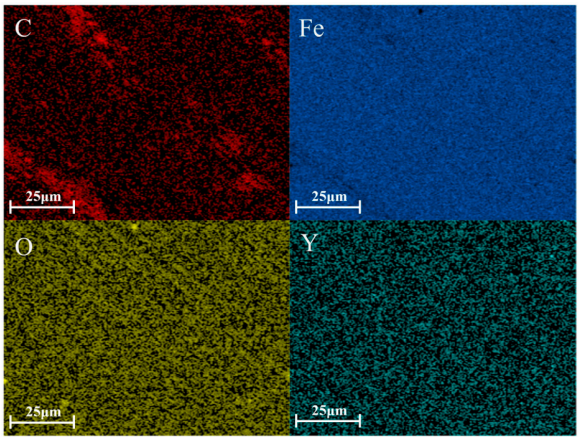

Figure 14. EDS spectrum of the worn surface under 100 N and 400 rpm with CD lubricant.

4. Discussion

The tribological behavior of the Y_2BaCuO_5 (Y211)-based lubricant system demonstrated a complex interplay between friction reduction, wear mitigation, and load responsiveness. Under low-load conditions (e.g., 100 N), the Y211-enhanced lubricant exhibited significantly lower coefficients of friction and wear rates compared to the neat PAO6 base oil. This improvement is primarily attributed to the formation of a stable boundary lubrication film facilitated by the uniform dispersion of ceramic particles. As confirmed by SEM and 3D confocal surface profilometry, the presence of Y211 resulted in smoother wear surfaces, fewer abrasive features, and reduced wear depths. The nanometric size and moderate surface activity of Y211 likely enabled it to function as a micro-scale rolling element or film-supporting filler, thereby distributing contact stresses and minimizing interfacial shear.

However, the friction and wear behavior exhibited pronounced load-dependent characteristics, with the tribological advantages of the Y211 additive diminishing as the applied normal load exceeded 200 N. This decline is likely attributable to the mechanical degradation of the lubricant film under elevated contact pressures, potentially resulting in additive squeeze-out or insufficient particle replenishment at the sliding interface. Although the additive continued to suppress the coefficient of friction to some extent under moderate loads (300–400 N), its advantage in wear resistance became increasingly marginal. These findings suggest a transition in the lubrication mechanism from additive-dominated behavior to base oil-dominated behavior as the load increases, highlighting the critical role of film integrity and particle retention under mechanical stress.

Compared to conventional additives such as TiO_2 and graphite, Y_2BaCuO_5 (Y211) offers distinct advantages in thermal stability and ceramic interfacial compatibility. However, its limited tribo-chemical reactivity may hinder its performance under high-pressure conditions, suggesting the need for surface functionalization to enhance adhesion and promote effective film formation. And for comparison, Gao et al. reported that dialkyldithiophosphate-functionalized MXene nanosheets achieved a 35% reduction in the coefficient of friction (COF) under a 40 N load. In contrast, the Y211-based lubricant demonstrated a more substantial COF reduction of approximately 55% under a 100 N load, although its performance declined at higher loads. Unlike two-dimensional MXenes, which primarily rely on interlayer slippage to reduce friction, the friction-reducing effect of Y211 is more likely attributed to micro-rolling and interfacial filling mechanisms associated with its ceramic particle structure. Future research should consider surface modification of Y211 particles or hybridization with soft-phase materials to optimize the composite's lubricating properties. In addition, in situ observation techniques and surface-sensitive spectroscopic analyses (e.g., X-ray photoelectron spectroscopy, Raman spectroscopy) could be employed to elucidate the additive–substrate interactions and identify potential tribochemical mechanisms responsible for the observed performance behavior.

5. Conclusions

This study investigated the tribological performance of the high-temperature superconductor precursor Y_2BaCuO_5 (Y211) when employed as a novel lubricant additive in PAO6 base oil. High-purity Y211 powder was successfully synthesized via chemical coprecipitation, exhibiting high phase purity and well-defined morphology. Subsequently, a lubricant system (designated CD) containing 0.3 wt.% Y211 dispersed in PAO6 was prepared, which demonstrated excellent dispersion stability and redispersibility. Utilizing a custom-designed end-face friction testing apparatus, the frictional behavior of this lubricant system was systematically investigated and benchmarked against that of neat PAO6 base oil under varying load conditions (100–500 N) and rotational speeds (300–500 rpm).

The experimental findings revealed the following:

Friction Reduction Capability of Y211: Compared to the neat PAO6 base oil, the CD lubricant containing 0.3 wt.% Y211 powder consistently exhibited superior friction-reducing performance, resulting in a lower overall coefficient of friction.

Load Dependency: The friction-reducing effectiveness of the Y211 additive displayed a pronounced dependence on the applied load. Under lower load conditions (e.g., 100 N), the CD lubricant exhibited a significantly lower COF than pure PAO6, highlighting its strong anti-friction effect. However, as the load increased, the COF followed a complex, non-linear trend: initially rising and peaking at 200 N, then declining slightly, and eventually stabilizing. When the load exceeded 200 N, the friction-reducing advantage of the CD lubricant diminished or disappeared altogether, with the COF approaching that of the base oil. This behavior is likely due to the partial squeeze-out of the lubricant medium from the friction interface under high pressure, which may hinder the effective infiltration and action of Y211 particles at the tribological interface. As a result, the lubrication regime becomes increasingly dependent on the intrinsic film-forming ability of the base oil.

Influence of Rotational Speed: Within the tested speed range (300–500 rpm), variations in rotational speed exerted a relatively minor effect on the friction coefficients of both the CD lubricant and the neat PAO6. Although a slight decreasing trend in the friction coefficient was observed at higher speeds, the applied load was identified as the more dominant factor influencing tribological performance.

Base Oil Stability: The neat PAO6 base oil exhibited stable frictional behavior across the tested load and speed conditions, consistently maintaining a friction coefficient of approximately 0.1.

In summary, this study provides a preliminary validation of the feasibility of employing Y211 powder as a lubricant additive, highlighting its significant friction-reducing potential, particularly under low-load operating conditions. However, the limited performance observed at higher loads underscores the necessity for further investigation into its underlying tribological mechanism. Future efforts could focus on optimizing additive concentration, enhancing dispersion stability, or implementing surface modifications to bolster its lubricating efficacy across a broader spectrum of operating conditions. This research offers novel insights and experimental grounding for the cross-disciplinary application of Y211, a material traditionally associated with superconductivity, within the field of tribology, thereby holding a significant exploratory value. Subsequent work should encompass detailed wear scar analysis, elucidation of tribo-chemical mechanisms, and performance assessments under more demanding operational environments.

Author Contributions: Conceptualization, J.X.; methodology, S.C. and L.H.; formal analysis, J.X. and S.C.; investigation, J.X. and S.C.; data curation, S.C. and L.H.; writing—original draft preparation, S.C.; supervision, J.X.; project administration, J.X.; funding acquisition, J.X.; All authors have read and agreed to the published version of the manuscript.

Funding: This research was funded by the National Natural Science Foundation of China (Grant No. 52411540029 and 52175165) and the Fundamental Research Funds for the Central Universities (JZ2025HGTG0268).

Data Availability Statement: The original contributions presented in this study are included in the article; further inquiries can be directed to the corresponding author.

Conflicts of Interest: The authors declare no conflicts of interest.

References

1. Olabi, A.G.; Elsaid, K.; Sayed, E.T. Application of nanofluids for enhanced waste heat recovery: A review. *Nano Energy* **2021**, *84*, 105871. [CrossRef]
2. Zhang, F.; Yang, K.; Liu, G. Recent advances on graphene: Synthesis, properties and applications. *Compos. Part A Appl. Sci. Manuf.* **2022**, *160*, 107051. [CrossRef]
3. Farfan-Cabrera, L.I. Tribology of electric vehicles: A review of critical components, current state and future improvement trends. *Tribol. Int.* **2019**, *138*, 473–486. [CrossRef]
4. Holmberg, K.; Erdemir, A. The impact of tribology on energy use and CO_2 emission globally and in combustion engine and electric cars. *Tribol. Int.* **2019**, *135*, 389–396. [CrossRef]
5. Kalin, M.; Polajnar, M.; Kus, M. Green Tribology for the Sustainable Engineering of the Future. *J. Mech. Eng./Stroj. Vestn.* **2019**, *65*, 709–727. [CrossRef]
6. Stolarski, T.A. *Modern Tribology Handbook: Volume 2-Materials, Coating, and Industrial Applications*; Bhushan, B., Ed.; CRC Press: Boca Raton, FL, USA, 2001.
7. Liu, S.; Jing, Y.; Zhang, T. Excellent tribological and anti-corrosion performances enabled by novel hollow graphite carbon nanosphere with controlled release of corrosion inhibitor. *Chem. Eng. J.* **2021**, *412*, 128648. [CrossRef]
8. Manu, B.R.; Gupta, A.; Jayatissa, A.H. Tribological properties of 2D materials and composites—A review of recent advances. *Materials* **2021**, *14*, 1630. [CrossRef] [PubMed]
9. Gao, J.; Du, C.F.; Zhang, T. Dialkyl Dithiophosphate-Functionalized $Ti_3C_2T_x$ MXene Nanosheets as Effective Lubricant Additives for Antiwear and Friction Reduction. *ACS Appl. Nano Mater.* **2021**, *4*, 11080–11087. [CrossRef]
10. Xu, J.; He, R.; Zhang, C. The remarkable difference in water wettability of $YBa_2Cu_3O_7-x$ and Y_2BaCuO_5 powders. *Phys. C Supercond. Its Appl.* **2019**, *561*, 24–29. [CrossRef]
11. Huang, Z.; Ruiz, H.S.; Coombs, T.A. Pulsed field magnetization strategies and the field poles composition in a bulk-type superconducting motor. *Phys. C Supercond. Its Appl.* **2017**, *534*, 73–81. [CrossRef]
12. Xu, J.; Yuan, X.; Zhang, C. Dynamic Characteristics of High-T_c Superconductor and Hydrodynamic Fluid-Film Compound Bearing for Rocket Engine. *IEEE Trans. Appl. Supercond.* **2016**, *26*, 3600505.
13. Arai, Y.; Seino, H.; Yoshizawa, K. Development of superconducting magnetic bearing with superconducting coil and bulk superconductor for flywheel energy storage system. *Phys. C Supercond.* **2013**, *494*, 250–254. [CrossRef]
14. Zhang, C.P.; Yu, Z.M.; Wang, J.R. YBCO bulk superconductors prepared by top-seed PMP process. *Phys. C Supercond.* **2003**, *386*, 231–235. [CrossRef]
15. Tepe, M.; Uzun, Y.; Gokay, U.S. Superconducting Properties of Melt-Textured Growth $YBa_2Cu_3O_{7-x}$ Materials with Y211 Addition. *J. Supercond. Nov. Magn.* **2015**, *28*, 541–544. [CrossRef]
16. Mucha, J.; Rogacki, K.; Misiorek, H. Influence of the Y211 phase on anisotropic transport properties and vortex dynamics of the melt-textured Y123/Y211 composites. *Phys. C Supercond. Its Appl.* **2010**, *470*, S1009–S1010. [CrossRef]
17. Xu, K.X.; Wu, X.; Qiu, J. Observations of the influence of Y-211 inclusions on melt textured growth of single domain Y–Ba–Cu–O. *Supercond. Sci. Technol.* **2007**, *20*, 969. [CrossRef]
18. Serradilla, I.G.; Calleja, A.; Capdevila, X.G. Synthesizing the Y-123/Y-211 composite by the PVA method. *Supercond. Sci. Technol.* **2002**, *15*, 566. [CrossRef]
19. Fang, Y.; Danyluk, S. Coefficients of friction of YBCO-YBCO and YBCO-Ag ball-on-flat couples. *J. Mater. Sci.* **1993**, *28*, 5658–5662. [CrossRef]
20. Fernandez, F.; Colon, C.; Duran, A. The Y_2BaCuO_5 oxide as green pigment in ceramics. *J. Alloys Compd.* **1998**, *275*, 750–753. [CrossRef]
21. Zhou, L.; Chen, S.K.; Wang, K.G.; Zhang, P.X.; Feng, Y. Synthesis of ultrafine Y_2BaCuO_5 powder and its incorporation into YBCO bulk by powder melting process. *Phys. C Supercond.* **2001**, *363*, 99–106. [CrossRef]
22. Rotta, M.; Namburi, D.K.; Shi, Y. Synthesis of Y2BaCuO5 nano-whiskers by a solution blow spinning technique and their successful introduction into single-grain, YBCO bulk superconductors. *Ceram. Int.* **2019**, *45*, 3948–3953. [CrossRef]
23. Bhargava, A.; Mackinnon, I.D.R.; Yamashita, T. Bulk manufacture of YBCO powders by coprecipitation. *Phys. C Supercond.* **1995**, *241*, 53–62. [CrossRef]
24. Shter, G.E.; Grader, G.S. YBCO oxalate coprecipitation in alcoholic solutions. *J. Am. Ceram. Soc.* **1994**, *77*, 1436–1440. [CrossRef]
25. Li, F.; Vipulanandan, C. Characterization of Y_2BaCuO_5 nanoparticles synthesized by nano-emulsion method. *J. Nanopart. Res.* **2007**, *9*, 841–852. [CrossRef]
26. Antončík, F.; Sedmidubský, D.; Jiříčková, A. Thermodynamic properties of stoichiometric non-superconducting phase Y_2BaCuO_5. *Materials* **2019**, *12*, 3163. [CrossRef] [PubMed]
27. Roa, J.J.; Capdevila, X.G.; Martínez, M.; Espiel, F.; Segarra, M. Nanohardness and Young's modulus of YBCO samples textured by the Bridgmantechnique. *Nanotechnology* **2007**, *18*, 385701. [CrossRef]

28. Peña-Parás, L.; Gao, H.; Maldonado-Cortés, D.; Vellore, A.; García-Pineda, P.; Montemayor, O.E.; Nava, K.L.; Martini, A. Effects of substrate surface roughness and nano/micro particle additive size on friction and wear in lubricated sliding. *Tribol. Int.* **2018**, *119*, 88–98. [CrossRef]
29. Serre, I.; Pradeilles-Duval, R.M.; Celati, N. Tribological and corrosion experiments of graphite ring against Ti–6Al–4V disk: Influence of electrochemical and mechanical parameters. *Wear* **2006**, *260*, 1129–1135. [CrossRef]
30. Zheng, C.; Hirayama, T.; Yamashita, N.; Gu, H.; Wang, W.; Liu, K.; Xu, J. Underlying mechanisms of improved cryogenic tribological performance of pure graphite: Suppressed thermal atomic motions and enhanced mechanical properties. *J. Tribol.* **2025**, *147*, 122101. [CrossRef]
31. Zheng, C.; Zhang, C.; Sun, W.; Wang, W.; Liu, K.; Xu, J. Experiments and molecular dynamic simulations on the cryogenic tribological behaviors of pure silver in liquid nitrogen. *Tribol. Int.* **2023**, *188*, 108836. [CrossRef]

Disclaimer/Publisher's Note: The statements, opinions and data contained in all publications are solely those of the individual author(s) and contributor(s) and not of MDPI and/or the editor(s). MDPI and/or the editor(s) disclaim responsibility for any injury to people or property resulting from any ideas, methods, instructions or products referred to in the content.